Characterization of displacement forces and image artifacts in the presence of passive medical implants in low-field (< 100 mT) permanent magnet-based MRI systems, and comparisons with clinical MRI systems

Speybroeck, C.D.E. van; O'Reilly, T.; Teeuwisse, W.; Arnold, P.M.; Webb, A.G.

Physica Medica 84 (2021) 116–124

Contents lists available at ScienceDirect

Physica Medica

journal homepage: www.elsevier.com/locate/ejmp

Original paper

Characterization of displacement forces and image artifacts in the presence of passive medical implants in low-field (<100 mT) permanent magnet-based MRI systems, and comparisons with clinical MRI systems

C.D.E. Van Speybroeck [a,1], T. O'Reilly [a,1], W. Teeuwisse [a], P.M. Arnold [b], A.G. Webb [a,*]

[a] CJ Gorter Center for High Field MRI, Department of Radiology, Leiden University Medical Center, Leiden, the Netherlands
[b] Department of Neurosurgery, Carle Foundation Hospital, Urbana. IL 61801, USA

ARTICLE INFO

Keywords:
Low-field MRI
Image artifacts
Displacement forces
MR safety
Passive implants

ABSTRACT

Purpose: To investigate the displacement forces and image artifacts associated with passive medical implants for recently-developed low-field (<100 mT) MRI systems, and to compare these with values from higher field strengths used for clinical diagnosis.
Methods: Setups were constructed to measure displacement forces in a permanent magnet-based Halbach array used for in vivo MRI at 50 mT, and results compared with measurements at 7 T. Image artifacts were assessed using turbo (fast) spin echo imaging sequences for four different passive medical implants: a septal occluder, iliac stent, pedicle screw and (ferromagnetic) endoscopic clip. Comparisons were made with artifacts produced at 1.5, 3 and 7 T. Finally, specific absorption rate (SAR) simulations were performed to determine under what operating conditions the limits might be approached at low-field.
Results: Displacement forces at 50 mT on all but the ferromagnetic implant were between 1 and 10 mN. Image artifacts at 50 mT were much less than at clinical field strengths for all passive devices, and with the exception of the ferromagnetic clip. SAR simulations show that very long echo train (>128) turbo spin echo sequences can be run with short inter-pulse times (5–10 ms) within SAR limits.
Conclusions: This work presents the first evaluation of the effects of passive implants at field strengths less than 100 mT in terms of displacement forces, image artifacts and SAR. The results support previous claims that such systems can be used safely and usefully in challenging enviroments such as the intensive care unit.

1. Introduction

Magnetic resonance imaging (MRI) is a valuable, non-invasive and widely applicable imaging technique. Tens of millions of scans are performed world-wide each year. Standard clinical field strengths are 1.5 and 3 Tesla, corresponding to operating frequencies of ~ 63.5 and ~ 127 MHz, respectively. Normal operation involves transmission of kilowatts of power from a body coil built into the bore of the magnet, with signal reception via a close-fitting multi-element array of receiver coils. Since MR imaging involves placing the patient in a strong static magnetic field, transmitting several kilowatts of power into the patient, and rapid switching of secondary magnetic fields (produced by the gradient coils), there are a number of potential safety issues involved in clinical scanning. If implanted devices contain ferromagnetic components, they can constitute a safety hazard due to rotational and translational forces on the implant when the patient enters the MRI through the strong spatial static magnetic field gradient. If the medical implant, or associated connecting wires, has a dimension that is a substantial fraction of the wavelength of the transmitted radiofrequency (RF) power, there is the possibility of tissue heating and damage due to the interaction of the RF energy and the implant [1]. In order to allow safe MRI scanning, a substantial number of federal/international guidelines must be adhered to, including the magnetically-induced displacement force F_m and the specific absorption rate (SAR) [2]. In addition, if implanted medical devices are metallic, their interaction with the static magnetic field can cause image artifacts which substantially reduce the diagnostic quality of the scan, altering the risk/benefit analysis for the patient.

* Corresponding author.
E-mail address: a.webb@lumc.nl (A.G. Webb).
[1] denotes equal contributions as first author.

https://doi.org/10.1016/j.ejmp.2021.04.003
Received 2 February 2021; Received in revised form 27 March 2021; Accepted 6 April 2021
Available online 21 April 2021

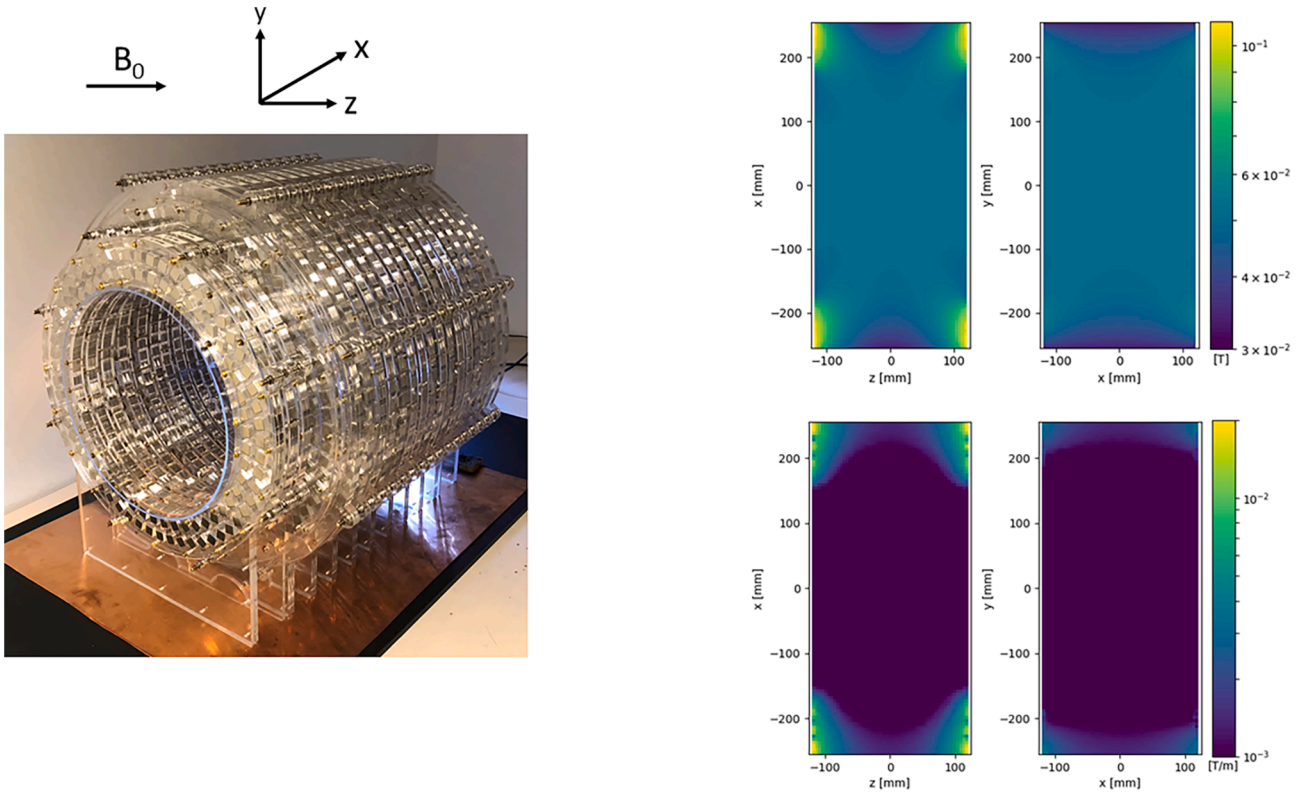

Fig. 1. (left) Photograph of the 50 mT Halbach array magnet with clear bore diameter of 27 cm. The x, y and z spatial convention is also shown (top right) Simulated magnetic field through the central axes of the magnet in the yx and zx planes. (bottom right) Corresponding calculated plots of the spatial gradient of the magnetic field.

One disadvantage of MRI as a clinical imaging modality is the expense of system, both in terms of purchase cost and continued maintenance. The magnet must be housed in an RF shielded room, and its operation requires highly-trained technicians [3–5]. These factors limit its use to late in the healthcare cycle, and its siting to major hospitals. As a result it plays little role in screening in the developed world, and it is estimated that worldwide ~ 70% of the population has zero access to an MRI scan [6,7]. Within the past five years there has been a strong push, academically and commercially, to address this issue by developing low-field (less than100 mT) MRI systems that have been designed for use in the intensive care unit (ICU) [8,9], for pediatric imaging in developing countries [10,11] and as point-of-care devices [12]. Each of these systems is based upon permanent magnet technology, using variously a yoked C-shape magnet [8,9], a homogeneous Halbach configuration [10,11], or a gradient Halbach configuration [13–15].

The advantages of low-field MRI include reduced patient contraindications, more benign image artifacts, and low SAR, which allows efficient data acquisition using, for example, long echo trains of fully-refocused turbo (fast) spin echoes (TSE). However, there are currently very few if any published quantitative assessments of these safety aspects or comparisons to standard clinical systems. The American Society for Testing and Materials (ASTM) and the National Electrical Manufacturers Association (NEMA) have written multiple quantification protocols on these aspects; however, many of these protocols cannot be directly applied to a Halbach array MRI system due to the transverse direction of the main magnetic field B_0, and the limited size of the bore, i.e. currently head-only as opposed to whole-body. THis study provides the first quantitative results for magnetically induced forces and image artifacts from passive medical devices with different geometries and susceptibilities on a 50 mT Halbach-based system, also discussing adaptations of ASTM protocols. In addition we simulate the SAR in terms of parameters such as echo train length and inter-pulse times for TSE sequences.

2. Materials and Methods

The system used in this study, operating at 50 mT (2.15 MHz), has been described in detail previously [11] and consists of a Halbach magnet of twenty three rings stacked 22 mm apart, with two layers of N48 neodymium boron iron (NdBFe) magnets ($12 \times 12 \times 12$ mm^3) per ring. The array has a clear bore of 27 cm, and a length of 50 cm between the two outer rings. An additional shim ring filled using $3 \times 3 \times 3$ mm

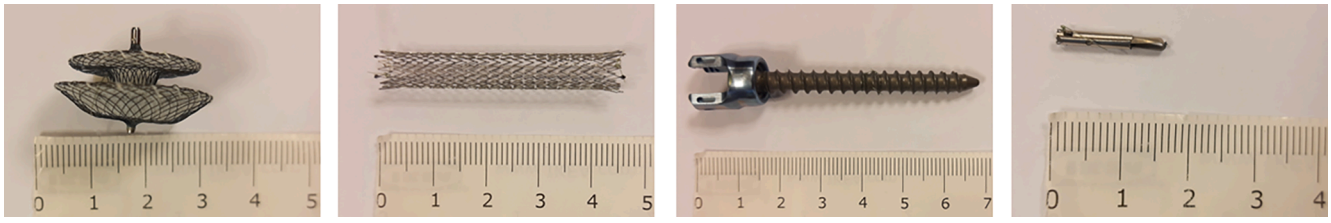

Fig. 2. Photographs of the four passive implants used to quantify image artifacts. (left to right) A septal occluder, an iliac stent, a pedicle screw, and an endoscopic clip. The scale is in centimeters.

Fig. 3. (left) The setup for the magnetically induced displacement force measurement inside the 50 mT system with the angle of deflection α', angle of rotation β and absolute angle of deflection α indicated. The setup is based on the F2052-15 ASTM protocol with the additional capability of rotating the device to enable measurement of the variation along the z-axis. (b) The setup used for comparison measurements on the 7 T system follows the F2052-15 ASTM protocol.

N45 NdBFe magnets is used to improve the B_0 field homogeneity: the value achieved was 2400 parts-per-million (ppm) over a 20 cm diameter spherical volume (DSV). The total weight of the magnet, including all components, is ~ 75 kg. Fig. 1 shows a photograph of the magnet, the simulated magnetic field through the central plane in two axes, and the corresponding calculated spatial gradient of the static magnetic field. The magnet is positioned inside a 62.5 × 62.5 × 85 cm Faraday cage constructed from 2 mm thick aluminium sheets. Gradients coils consist of 1.5 mm diameter copper wire pressed and glued into 3D printed formers. The efficiencies of the ×, y and z gradient coils are 0.59, 0.95 and 1.02 mT/m/A, respectively [16]. A triple-axis custom-designed gradient amplifier produces an output gain of 1.5 Amps per 1 V input from the +/- 10 V 16-bit digital-to-analogue (DAC) gradient drivers of the MR console (Magritek Kea 2, Aachen, Germany). The RF pulses generated by the MR console are amplified by a custom built 1 kW RF amplifier. All experiments on the 50 mT system use a 15 cm diameter, 15 cm long solenoid transmit/receive coil made with 45 turns of 0.8 mm diameter copper wire.

Four implants, shown in Fig. 2, were used in this study with a wide range of magnetic susceptibilities: a septal occluder (Amplatzer, nitinol), an Iliac stent (Cordis, S.M.A.R.T. Control, nitinol), a pedicle screw (CD Legacy 5.5, Medtronic, stainless steel, non-ferromagnetic) and an endoscopic clip (Resolution, Boston Scientific, stainlesss steel, ferromagnetic). We note that, since it is ferromagnetic, the endoscopic clip lies outside the remit of the ASTM protocol [17], which only covers MR-Conditional and MR-Safe implants, but is included here as an illustrative example.

For comparison purposes, images were also acquired from clinical 1.5, 3 and 7 Tesla whole body MRI systems (Philips Healthcare, Best, The Netherlands). Displacement forces were also measured on the 7 Tesla system, following the procedure outlined by van Rijn et al. [18,19]. Images for artifact assessment were acquired using body coil transmit and head array receive (1.5 and 3 T) and head coil transmit and head array receive (7 T).

2.1. Magnetically induced displacement forces arising from passive medical implants

The assessment of magnetically induced displacement forces, F_m, of medical devices is described in ASTM protocol F2052-15 [20]. Summarizing, the device is suspended by a string near the entrance to, and on the main axis of, the bore of the MRI scanner. The string should be less than 1% of the weight of the device and should be long enough such that the device hangs freely. The spatial gradient of the static magnetic field should be within 20% of its on-axis maximum. The angular deflection of the device is measured using a protractor with 1° markings. The angle of deflection, α, provides the relation between F_m (which is proportional to the spatial gradient of B_0) and F_g, the gravitational force: $F_m = F_g \tan\alpha$. The device must be on-axis with the bore to determine this relation, since the protocol is based on the concept that on axis the gradient vector field of the scalar B_0 is $\nabla\left|\vec{B}_0\right| = \frac{d\left|\vec{B}_0\right|}{dz}\hat{z}$.

However, in the case of the Halbach array magnet, the gradient must be considered in two directions: $\nabla\left|\vec{B}_0\right| = \frac{d\left|\vec{B}_0\right|}{dx}\hat{x} + \frac{d\left|\vec{B}_0\right|}{dz}\hat{z}$. The third component in the y-direction is not taken into account, since F_g acts along this axis. Unlike for a conventional superconducting magnet, the maximum of the spatial gradient is not located along the central axis but at a certain radial distance (Fig. 1), and so we adapted the protocol by designing a custom-built apparatus, shown in Fig. 3, which can rotate to sample different radial locations (we note that a conventional flat support would limit the size, and thus the accuracy, of the measurements since the bore of the 50 mT is much smaller than that of clinical scanners). For comparison measurements at 7 T, the standard ASTM protocol is used [18]. On both systems, the measurement was made in the region of highest spatial gradient at the entrance of the bore. The angle of deflection α was measured for the pedicle screw, iliac stent and endoscopic clip outlined earlier, as well as a glucose sensor (Freestyle Libre, Abbott) and four different dental retainer wires (Pentacat, Penta One, Forestaflex and Remanium) which have been studied at 7 T previously [19]. For objects exceeding a 45° angle of deflection, a non-magnetic (brass) weight was added, according to the method proposed by New, et al. [21].

2.2. Image artifacts arising from passive medical implants

ASTM F2119-07 [17] quantifies image artifacts produced by implants by acquiring a pair of images with and without an implant in the field-of-view. This implant should be immersed in a solution, preferably $CuSO_4$-doped water to reduce T_1, and the container which holds both the implant and solution should be large enough to have at least 4 cm clearance around the implant. A reference object that causes no image artefacts itself, for example a nylon rod, should be placed in the

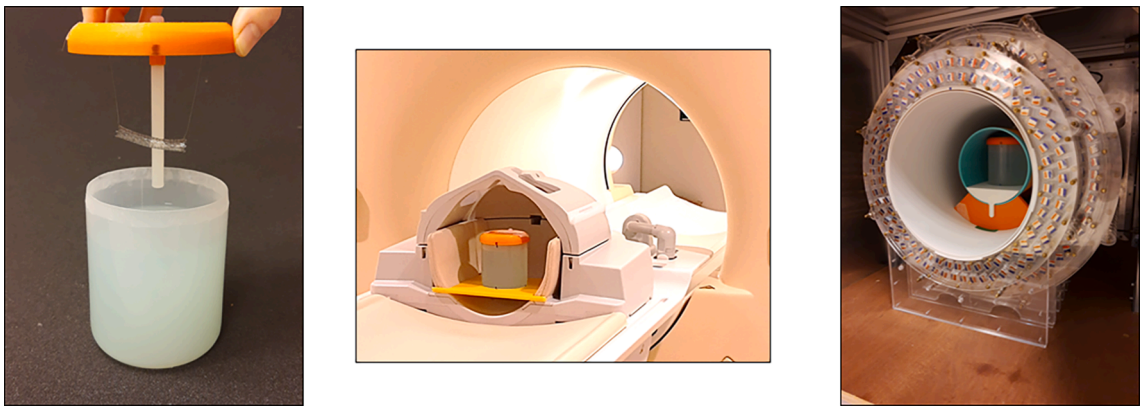

Fig. 4. (left) Photograph of the set up used for measurement of image artifacts. A cylindrical container is filled with $CuSO_4$ doped water. The lid integrates a solid nylon rod and the particular device is attached using thin nylon string, and located in the centre of the cylinder. A 3D printed former was designed to locate the phantom in the centre of the magnet for reproducible positioning. (centre) and (right) illustrations of the physical set up on the 3 T and 50 mT systems, respectively.

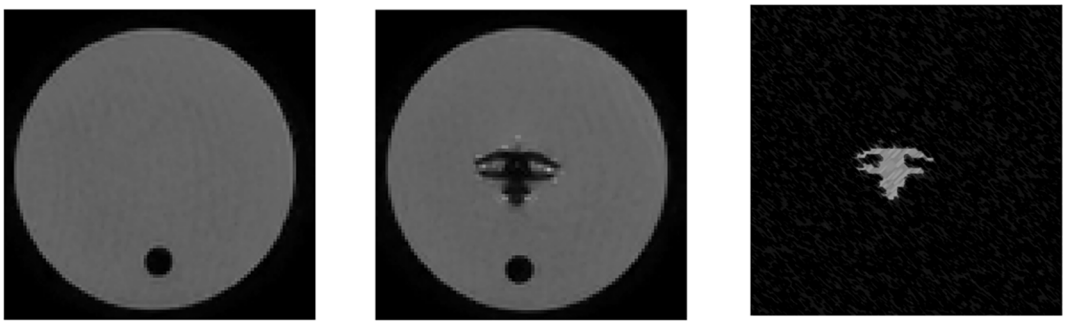

Fig. 5. Schematic showing the processing steps involved in quantifying the artifact size. (left) Reference image acquired with the nylon rod present as a black hole. (centre) Image acquired with implant in place. (right) After correction for any slight positional changes and intensity normalization, the pixels showing $>$ 30% change in intensity are displayed, and summed to give the total number of pixels which constitute the artifact size.

container and must be present in both images. Images should be made of the implant in all relevant (i.e. depending on the degree of cylindrical symmetry of the implant) orientations relative to B_0. For all orientations, images should be made with all possible phase- and frequency-encoding directions. For the worst-case orientation, and corresponding worst-case phase- and frequency-encoding combination, a gradient echo image is also acquired.

Fig. 4 shows the setup for the measurements. The container (polypropylene bottle, diameter 9 cm, height 11 cm) contains a nylon reference rod, placed next to the implant, and is filled with $CuSO_4$ solution. The implants were attached to thin nylon strings such that they are located in the middle of the container. The reference rod was fixed at the edge of the container, leaving as much space around the implant as possible. Images were acquired in every unique combination of frequency- and phase-encoding direction with respect to B_0. Since all the used objects were cylindrical symmetric, two sets of scans (swapping phase and frequency directions) were run for each implant.

Imaging experiments were performed on the 50 mT scanner as well as a commercial 1.5 T, 3 T and 7 T scanners (Philips, Best, the Netherlands). In the first set of experiments, the imaging parameters were set to be as close to identical as possible on all four systems, paying particular attention to the acquisition bandwidth (Hz per pixel) which is the major determinant of image artifact size for a given field strength. In this case a bandwidth of 160 Hz/pixel was used, based on typical imaging parameters used on the 50 mT system. On all systems the spatial resolution was $1 \times 1 \times 1$ mm, a 3D non-selective TSE sequence was used with no signal averaging. First order shimming was performed prior to every scan on the phantom without an implant placed in it, the same shim settings were subsequently used for imaging with the implants in the phantom.

Since a 160 Hz/pixel bandwidth is well below the maximum attainable on the clinical systems, the second set of experiments acquired images with a much higher bandwidth (880 Hz/pixel) to more closely resemble standard clinical protocols.

The definition for an image pixel corresponding to an image artifact used in the ASTM protocol [17] is one whose intensity varies by at least 30% with respect to the corresponding intensity in the reference image containing the nylon rod only. As illustrated in Fig. 5, the number of distorted pixels is calculated by setting all the pixels to zero which are within 30% of the reference image, and summing the remaining pixels. This process is performed for the coronal slice containing the biggest artifact. In order to account for any slight differences in signal intensity between the two scans, normalization is performed for an area of the image where distortion does not occur. Any slight shift in position (~mm translation or rotation) between the two images produces "ring artifacts" around the outside of the cylinder and the nylon rod: these are masked out.

2.3. Simulated specific absorption rate for TSE sequences at low-field.

T_1 relaxation due to dipole–dipole interactions is more efficient at lower B_0 fields and this means that the optimum TR, in terms of maximizing SNR per square root time, is shorter at lower fields. This means that a greater degree of signal averaging can be used at lower field, thus increasing the SNR. T_2 relaxation times are relatively field-independent. At higher magnetic fields, when running TSE sequences, SAR often limits the minimum inter-pulse time, the maximum number of echoes acquired, and the tip angle of the "refocussing pulse". At lower field, this is much less of an issue, and TSE sequences with a large number of echoes, short inter-pulse time and full 180° refocusing pulses can be run, all of

Table 1
Summary of deflection angles and forces exerted on different passive implants at 7 T and 50 mT.

		7 T			50 mT		
Object	Weight (g)	Weight added (g)	Deflection angle (degrees)	Force on object (mN)	Weight added (g)	Deflection angle (Degrees)	Force on object (mN)
Iliac Stent	0.2	–	5	0	–	0	0
Penticle Screw	7.43	–	5	6.38	–	0	0
Pentacat wire	0.09	2	41	17.77	0.29	9	0.59
Penta One wire	0.09	2	43	19.02	0.29	10	0.66
Endoscopic Clip	0.1	4.5	37	34.00	0.98	11	2.06
Forestaflex wire	0.06	4.15	51	51.00	1.32	13	3.13
Remanium wire	0.08	4.15	56	61.50	1.9	21	7.46
Glucose Sensor	3.1	11.25	45	140.77	0.29	14	8.29

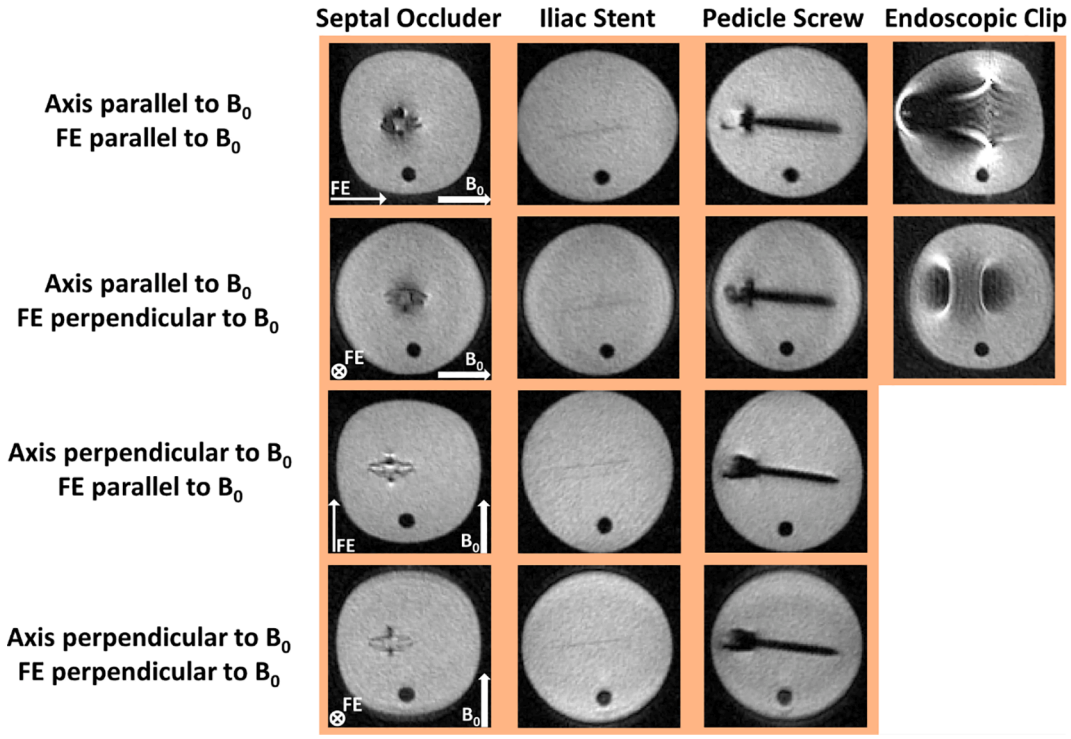

Fig. 6. Images through the centre of each object from a 3D TSE sequence on the 50 mT system with four different objects: the frequency encoding (FE) direction is specified in each case. Spatial resolution 1 × 1 × 1 mm and readout bandwidth 160 Hz per pixel.

which which increase the SNR. Most papers on low-field MRI simply state that SAR is not problematic at low-fields, given that the SAR is proportional to the square of the B_0 field. Nevertheless, it is clear that there must be some limits in terms of data acquisition parameters, beyond which SAR does indeed become an issue. In order to give some guidelines on how these values relate to SAR limits, we performed numerical simulations based on equations originally derived by Bottomley et al. [22] for a coil producing uniform excitation within the imaging region-of-interest:

$$SAR = 6.81 \times 10^{-19} \frac{\nu^2 R^2}{\rho s \mathrm{TR}} \sum_i \frac{N_i}{\tau_i} \left(\frac{2\theta_i}{\pi}\right)^2$$

where N_i represents the number of RF pulses applied, θ_i the tip angles of these pulses, τ_i the duration of each pulse; R is the radius of coil, ρ the resistivity of the imaged body part, and s its specific gravity. For simulations of the brain performed here, R has a value of 0.092 m, ρ2.17 Ωm, and s 1.07. Since TSE sequences are commonly used for portable low-field MRI systems, and also produce the highest SAR, we simulated different pulse durations, echo train lengths, and inter-pulse times. We specifically modelled scenarios which lie within the technical limits of most current low-field systems. Since most of these indeed result in SAR values which produce temperature rises which are well below the values required by the National Electrical Manufacturers Association (NEMA) protocol for the characterization of the specific absorption rate for magnetic resonance imaging systems [23], only simulations were performed. We also note that, since all medical implants are much smaller than the wavelength ($\lambda \approx 140$ m in air and 20 m if fully immersed in high water-content tissue) at 2.15 MHz, essentially identical values of SAR would be expected with or without a passive implant.

3. Results

3.1. Magnetically induced displacement forces

Table 1 lists the measured displacement angles and derived displacement forces acting on a range of different implants at 50 mT, and at 7 T to represent the other extreme of the highest magnetic field used clinically.

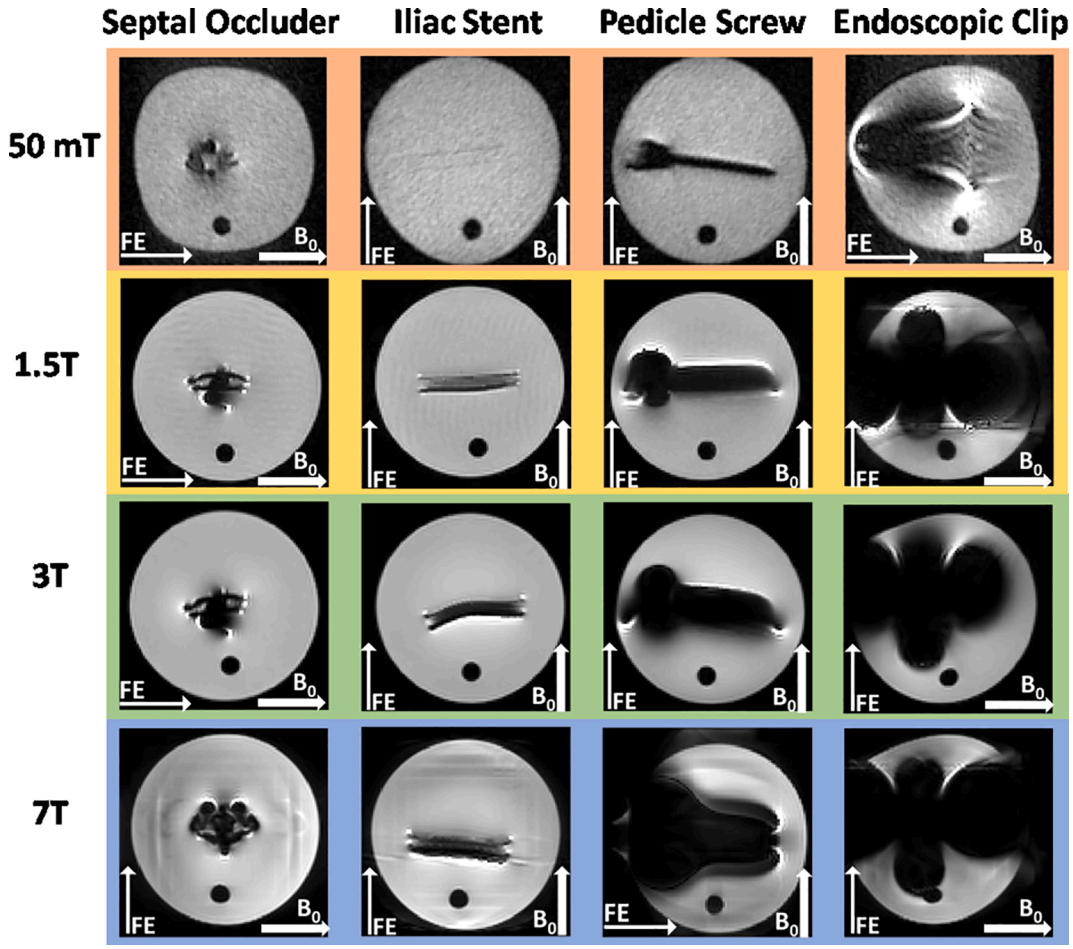

Fig. 7. Comparison of "worst-case" images for each object acquired at four different field strengths. Each image was acquired using a 3D turbo-spin echo sequence, spatial resolution 1 × 1 × 1 mm, readout bandwidth 160 Hz per pixel.

3.2. Image artifacts at 50 mT, 1.5 T, 3 T and 7 T.

Fig. 6 shows images acquired from four different implants on the 50 mT system using a TSE sequence with a readout bandwidth of 160 Hz per pixel. Four sets of images are shown, with the main axis of the implant parallel and perpendicular to B_0, and with the frequency and one of the phase encoding directions parallel and perpendicular to B_0. The images show that the artifact size is not greatly influenced by the orientation relative to B_0, nor by the orientation of the phase and frequency encoding directions. Note that since the endoscopic clip is ferromagnetic, it naturally aligns along the B_0 axis, and so there are no data for directions perpendicular to this.

Fig. 7 provides a direct comparison between the "worst-case" images (i.e. the largest artifact size as a function of object orientation with respect to B_0 and frequency/phase encoding axes) acquired on the 50 mT system with those acquired using the same acquisition bandwidth (160 Hz/pixel) on the 1.5, 3 and 7 Tesla human MRI scanners. In each of these scans, the worst case corresponds to the long axis of the device placed perpendicular to B_0, with the exception of the ferromagnetic clip which naturally aligns with B_0. As expected the image artifacts become larger the higher the value of B_0.

As outlined earlier, the clinical scanners have a much higher normal operational mode gradient strength (~40 mT/m) than is currently used on the 50 mT system (~8 mT/m), and so in practice a much higher pixel bandwidth than 160 Hz/pixel would be used when imaging patients with implants. Fig. 8 shows images corresponding to a bandwidth of ~ 880 Hz/pixel i.e. a bandwidth higher by a factor roughly equal to the difference in maximum gradient strengths. Even with the higher pixel bandwidth, the images acquired on the clinical systems show consistently higher artifacts compared to the low readout bandwidth images acquired on the 50 mT system.

Quantification of the artifact size was performed using the protocol outlined previously. Fig. 9 shows the artifact size obtained from both the best-case and worst-case situations for all four passive implants. Gradient echo images corresponding to the worst-case scenario are shown in the supplementary information. As expected the artifacts are greater in extent for the gradient echo compared to spin echo experiments. The images acquired at 50 mT, despite being relatively low in SNR due to the long echo time (15 ms) used, nevertheless show that there is still signal very close to (and even within) the implant in the cases of the septal occluder, iliac stent and pedicle screw, implying that rapid gradient echo sequences might also be feasible to run if the overall homogeneity of the B_0 field can be improved and sequence optimization performed to acquire gradient echo images with shorter echo times.

3.3. Simulations of specific absorption rate for TSE sequences at 50 mT

As mentioned earlier, most low-field systems acquire data based on extended TSE sequences with full 180° refocusing pulses (unlike at higher field strengths where pulses typically have much lower tip angles), which are either square [10,11] or amplitude and frequency modulated to provide sufficient excitation bandwidth [12,15]. For the 50 mT system used in this study, the typical MR linewidth (frequency spread) of a human head placed in the magnet is 1–2 kHz, meaning that an excitation pulse of 100–200 μs duration gives uniform excitation. Fig. 10 plots the SAR vs. inter-pulse delay for different echo train lengths

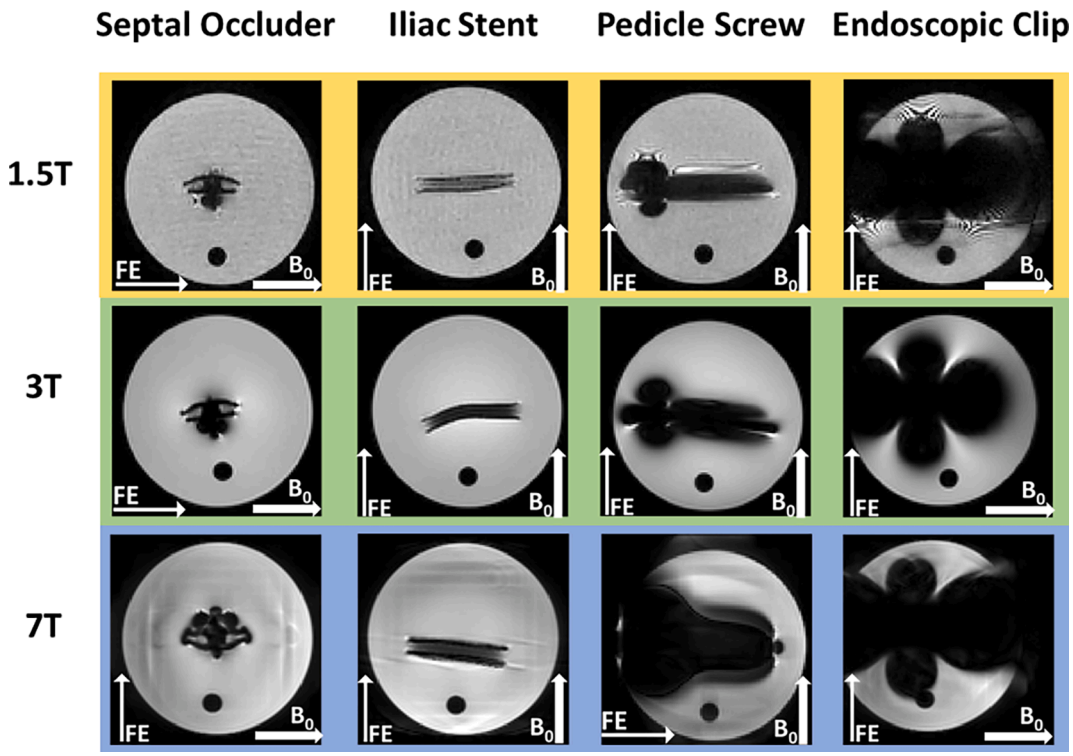

Fig. 8. Worst-case images acquired on each of the three clinical scanners with an increased readout bandwidth of 880 Hz per pixel.

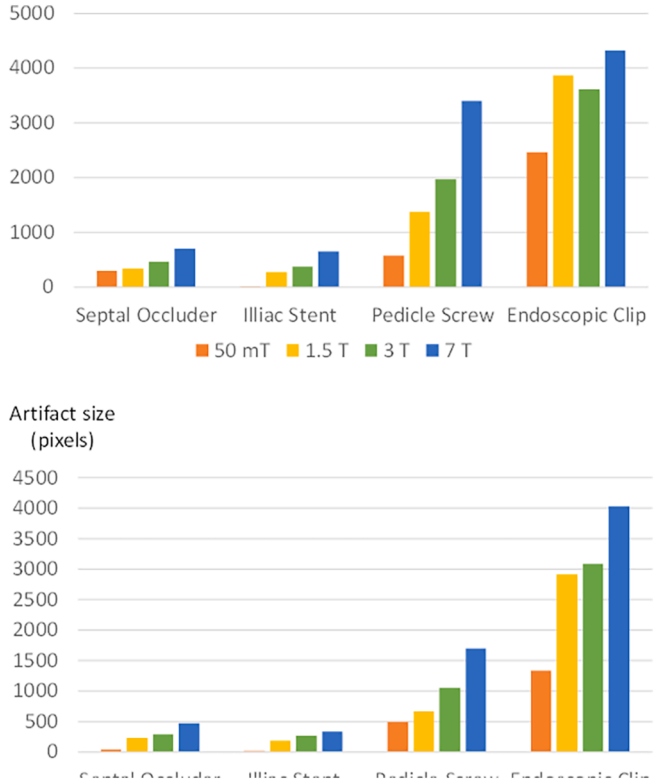

Fig. 9. Plots of the calculated image artifact size (1 pixel corresponds to 1 × 1 × 1 mm) for (top) the worst case and (bottom) the best case situation at all four field strengths.

of a TSE sequence, covering typical values reported in the literature, e.g. echo train lengths of 16–32 with inter-pulse times of ~ 10–20 ms. Under these conditions one can see that the SAR is roughly one order-of-magnitude lower than the allowed value [24] (assuming that there is no relaxation delay between successive k-space acquisitions, in which case the time-averaged SAR would be even lower). Only if one attempts to acquire large amounts of k-space in a single shot (ETL = 256 or 128) with an inter-pulse time of less than 10 ms, does the SAR approach the limit for the head [24]. Fig. 10 also shows the case for a much shorter RF pulse duration, corresponding to higher peak power. This scenario would be relevant if the static magnetic field was very inhomogeneous, for example when using surface magnets, and much shorter RF pulses were required to excite a much larger bandwidth. Fig. 10 shows that in the case of a 10 ms pulse, even typical echo train lengths (~32 echoes) with inter-pulse times (10–15 ms) can result in SAR values which are above the allowed limit.

4. Discussion

There has been a recent resurgence in interest in low-field MRI, driven by advances in readily-available magnetic materials with high remanence, improved magnetic-field modelling and optimization capabilities, and a realization that despite significant technical developments in MRI over the years the price and infrastructure required have essentially remained constant, making it still the most expensive clinical imaging modality, fully out of range for the vast majority of the world. In addition to this consideration, one of the areas in which low-field MRI has been postulated to make a signficant difference is in patients who cannot undergo a scan due to the presence of metallic materials, either as medical implants or as foreign objects as a result of penetrating trauma, usually shrapnel. In every case, there is a risk/benefit analysis for the patient which involves an evaluation of the safety of such a procedure versus the potential benefit, which is directly related to the attainable diagnostic image quality of the scan.

This study provides, to our knowledge, the first semi-quantitative overview of different safety aspects and analysis of image artifacts

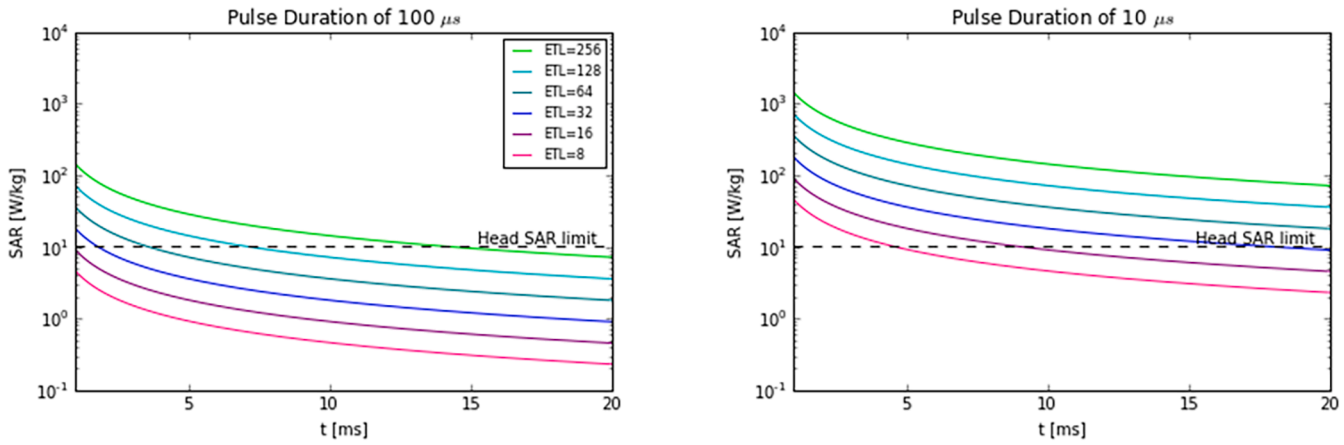

Fig. 10. Calculated specific absorption rate (SAR) as a function of the inter-pulse time (t) for a TSE sequence with different echo train lengths (ETLs). The pulse durations are (left) 100 μs and (right) 10 μs. The head SAR limit (10 W/kg) (24) is shown by the dashed line.

produced by various passive implants at low-field, in this case 50 mT, and compares the results to those obtained at conventional clinical field strengths (1.5 T and 3 T), as well as ultra-high field strength (7 T) for completeness. Since the size of medical implants and associated leads are much less than the RF wavelength, and gradient switching times are slower than those associated with clinical scanners, the main safety issue is the force from the static magnetic field, and the gradient in the static magnetic field. We note that, although most of these devices we assessed are used in conditions associated with organs other than the brain, and are therefore not directy applicable to many of the current (mainly neurological) studies performed at low-field, they represent situations which will be encountered as low-field systems expand into whole-body applications, and also represent some of the extremes of devices which will ultimately be encountered. In this work we only assessed translational forces, since these are higher than the rotational ones. The maximum translational force occurs in the region where the static magnetic field gradient is highest, while the maximum rotational forces occur in the region where the magnetic field is uniform and maximum, which is normally at the isocenter of the magnet. As shown by the values reported in Table 1, the translational forces for all the implants studies are very low, and so pose very little risk to the patient. Unlike in a conventional superconducting magnet, the patient's head is quite close to the inner bore of the magnet for most of the current low-field systems [8–10,12], and implants potentially have to travel through the relatively strong spatial gradients in the static magnetic field close to the outer bore of the magnet: therefore, we recommend that these types of measurement take place in these areas of high spatial gradients rather than along the bore of the magnet, which is the case for the ASTM protocols.

In terms of image quality, the size of image artifacts produced by medical implants is a highly non-linear function of field strength, and so in this study we included passive implants which produce relatively minor artifacts (iliac stent) up to one which is ferromagnetic and produces severe artifacts even at 50 mT (endoscopic clip). For the non-ferromagnetic implants, the TSE images at 50 mT show very little artifact around the implant, sometimes less than 1 pixel, with no "signal pile-up". This means that useful information can be obtained from tissue very close to the implant. As shown in Figs. 7 and 8, the image artifacts at 50 mT are substantially smaller than those at higher field strengths, even when much larger bandwidths are used at the higher fields. This study is limited in the sense that the results show the artifacts produced by simple TSE sequences. There are, of course, a number of techniques which have been developed for clinical systems to reduce "metallic artifacts" [25–27]. Using these types of sequence artifacts in the images acquired on the clinial scanners could potentially be reduced significantly, but these types of sequence do increase the scanning time at the particular field strength, and data acquisition parameters should ideally be optimized for each individual case: a detailed study and comparison could be the subject of a future study. Finally, it is important to note that implants which have substantial ferromagnetic components, or even magnetic ones such as cochlear implants, produce very large artifacts even at very low fields, resulting in images which will still be non-diagnostic.

The results of the SAR simulations suggest that under the vast majority of operating conditions limits will not be reached. TSE sequences with full refocussing pulses were analyzed, with different pulse durations, echo train lengths, and inter-pulse times – which can also be reformulated in terms of duty cycle and flip angle in terms of maximum power. As shown in Fig. 10, these limits might only be reached in cases where very short, very high power RF pulses have to be used to overcome very significant B_0 inhomogeneities.

In this study, we have looked at a relatively small number of implantable devices, and so we hope that the protocols developed will encourage other researchers to add to this list. Results were obtained at 50 mT since this represents the order-of-magnitude of magnetic field which is currently the focus for many academic and commercial groups, but it would be very instructive to consider higher field strengths (~0.2 T) associated with human field-cycling systems [28,29] and portable systems for extremity imaging [30].

5. Conclusion

Quantitative measures of displacement forces and image artifacts, as well as simulations of SAR, provide support for low-field MRI becoming a clinical imaging method for non-conventional settings such as the ICU and field hospitals dealing with head trauma, where conventional field strengths are inappropriate due to contra-indications. As discussed above, such low-field MRI systems may also constitute a low-budget solution for underdeveloped and/or developing countries.

Acknowledgement

Partial funding for this project was provided by Horizon 2020 European Research Grant FET-OPEN 737180 Histo MRI, Horizon 2020 ERC Advanced NOMA-MRI 670629, and a Simon Stevin Meester Prize.

Appendix A. Supplementary data

Supplementary data to this article can be found online at https://doi.org/10.1016/j.ejmp.2021.04.003.

References

[1] Park SM, Kamondetdacha R, Nyenhuis JA. Calculation of MRI-induced heating of an implanted medical lead wire with an electric field transfer function. J Magn Reson Imaging 2007;26(5):1278–85.

[2] Delfino JG, Woods TO. New Developments in Standards for MRI safety testing of medical devices. Curr RadiolReports 2016:4.

[3] Sarracanie M, Salameh N. Low-field MRI: How low can we go? A fresh view on an old debate. Front Phys-Lausanne 2020;8.

[4] Wald LL, McDaniel PC, Witzel T, Stockmann JP, Cooley CZ. Low-cost and portable MRI. J Magn Reson Imaging 2019.

[5] O'Reilly T, Webb A. Deconstructing and reconstructing MRI hardware. J Magn Reson 2019;306:134–8.

[6] Bhat SS, Fernandes TT, Poojar P, da Silva Ferreira M, Rao PC, Hanumantharaju MC, Ogbole G, Nunes RG, Geethanath S. Low-Field MRI of Stroke: Challenges and Opportunities. J Magn Reson Imaging 2020:e27324.

[7] Geethanath S, Vaughan Jr JT. Accessible magnetic resonance imaging: a review. J Magn Reson Imaging 2019.

[8] Sheth KN, Mazurek MH, Yuen MM, Cahn BA, Shah JT, Ward A, Kim JA, Gilmore EJ, Falcone GJ, Petersen N, Gobeske KT, Kaddouh F, Hwang DY, Schindler J, Sansing L, Matouk C, Rothberg J, Sze G, Siner J, Rosen MS, Spudich S, Kimberly WT. Assessment of Brain Injury Using Portable, Low-Field Magnetic Resonance Imaging at the Bedside of Critically Ill Patients. JAMA Neurol 2020.

[9] He Y, He W, Tan L, Chen F, F. M, Feng H, Xu Z. Use of 2.1 MHz MRI scanner for brain imaging and its preliminary results in stroke. J Magn Reson 2020;319:106829.

[10] O'Reilly T, Teeuwisse WM, de Gans D, Koolstra K, Webb AG. In vivo 3D brain and extremity MRI at 50 mT using a permanent magnet Halbach array. Magn Reson Med 2020.

[11] O'Reilly T, Teeuwisse WM, Webb AG. Three-dimensional MRI in a homogenous 27 cm diameter bore Halbach array magnet. J Magn Reson 2019;307.

[12] Cooley CZ, McDaniel P, Stockmann J, Srinivas SA, Cauley SF, Sliwiak M, Sappo C, Vaughn CF, Guerin B, Rosen MS, Lev MH, Wald LL. A portable brain MRI scanner for underserved settings and point-of-care imaging. arXiv:200413183 [eessIV] 2020.

[13] Cooley CZ, Haskell MW, Cauley SF, Sappo C, Lapierre CD, Ha CG, et al. Design of sparse halbach magnet arrays for portable MRI using a genetic algorithm. IEEE T Magn 2018;54(1).

[14] Cooley CZ, Stockmann JP, Armstrong BD, Sarracanie M, Lev MH, Rosen MS, et al. Two-dimensional imaging in a lightweight portable MRI scanner without gradient coils. Magn Reson Med 2015;73(2):872–83.

[15] Stockmann JP, Cooley CZ, Guerin B, Rosen MS, Wald LL. Transmit Array Spatial Encoding (TRASE) using broadband WURST pulses for RF spatial encoding in inhomogeneous B-0 fields. J Magn Reson 2016;268:36–48.

[16] de Vos B, Fuchs P, O'Reilly T, Webb A, Remis R. Gradient coil design and realization for a halbach-based MRI system. IEEE T Magn 2020;56(3).

[17] ASTM F2119-07 Standard Test Method for Evaluation of MR Image Artifacts from Passive Implants. 2007.

[18] van Rijn GA, Mourik JEM, Teeuwisse WM, Luyten GPM, Webb AG. Magnetic resonance compatibility of intraocular lenses measured at 7 Tesla. Invest Ophth Vis Sci 2012;53(7):3449–53.

[19] Wezel J, Kooij BJ, Webb AG. Assessing the MR compatibility of dental retainer wires at 7 Tesla. Magn Reson Med 2014;72(4):1191–8.

[20] ASTM F2052-15: Standard Test Method for Measurement of Magnetically Induced Displacement Force on Medical Devices in the Magnetic Resonance. 2015.

[21] New PFJ, Rosen BR, Brady TJ, Buonanno FS, Kistler JP, Burt CT, et al. Potential hazards and artifacts of ferromagnetic and nonferromagnetic surgical and dental materials and devices in nuclear magnetic-resonance imaging. Radiology 1983;147(1):139–48.

[22] Bottomley PA, Edelstein WA. Power deposition in whole-body Nmr imaging. Med Phys 1981;8(4):510–2.

[23] NEMA standards publication MS 8-2008. Characterization of the specific absorption rate for magnetic resonance imaging systems. 2008.

[24] International Electrotechnical Commission. Medical Electrical Equipment - Part 2-33: Particular Requirements for the Basic Safety and Essential Performance of Magnetic Resonance Equipment for Medical Diagnosis. 2015.

[25] Ben-Eliezer N, Solomon E, Harel E, Nevo N, Frydman L. Fully refocused multi-shot spatiotemporally encoded MRI: robust imaging in the presence of metallic implants. Magn Reson Mater Phys 2012;25(6):433–42.

[26] Gutierrez LB, Do BH, Gold GE, Hargreaves BA, Koch KM, Worters PW, et al. MR imaging near metallic implants using MAVRIC SL: initial clinical experience at 3T. Acad Radiol 2015;22(3):370–9.

[27] Koch KM, Lorbiecki JE, Hinks RS, King KF. A multispectral three-dimensional acquisition technique for imaging near metal implants. Magn Reson Med 2009;61(2):381–90.

[28] Broche LM, Ross PJ, Davies GR, Macleod MJ, Lurie DJ. A whole-body fast field-cycling scanner for clinical molecular imaging studies. Sci Rep-Uk 2019;9..

[29] Ross PJ, Broche LM, Lurie DJ. Rapid field-cycling MRI using fast spin-echo. Magn Reson Med 2015;73(3):1120–4.

[30] Nakagomi M, Kajiwara M, Matsuzaki J, Tanabe K, Hoshiai S, Okamoto Y, et al. Development of a small car-mounted magnetic resonance imaging system for human elbows using a 0.2 T permanent magnet. J Magn Reson 2019;304:1–6.